

Versatile Metamaterial: Exploring Symmetry-Protected Mode Resonances for Multi-Task Functionality

SOUHAILA BOUBLOUH,¹ MIGUEL SUAREZ,¹ GAO FENG,^{2,3}
 ABDERRAHMANE BELKHIR,⁴ ABDELKRIM KHELIF,^{3,5} AND FADI I.
 BAIDA^{1,*}

¹*Institut FEMTO-ST, UMR 6174 CNRS, Département d'Optique P. M. Duffieux, Université de Franche-Comté, 25030 Besançon Cedex, France*

²*University of Zhejiang, Hangzhou, Zhejiang, China*

³*Institut FEMTO-ST, UMR 6174 CNRS, Département MN2S, Université de Franche-Comté, 25030 Besançon Cedex, France*

⁴*Laboratoire de Physique et Chimie Quantique, Université Mouloud Mammeri, Tizi-Ouzou, Algeria*

⁵*College of Science and Engineering, Hamad Bin Khalifa University, Doha, Qatar*

**fbaida@univ-fcomte.fr*

Abstract: In this article, we present an experimental study supported by numerical modeling showing the possibility of exciting Symmetry-Protected Bound states In the Continuum (SP-BICs) in a 1D silicon grating fabricated on a lithium niobate substrate in both transverse electric and transverse magnetic polarization states of the incident illumination. This leads to different resonances in the transmission spectra with large quality factors up to 10^6 and a significant electric/magnetic field enhancement up to 10^5 opening the way to the exploitation of this structure for different sensing applications (biological, electromagnetic, thermal...) but also to nonlinear applications such as the generation of second harmonic, in addition to electro- and acousto-optic modulation.

© 2024 Optica Publishing Group

1. Introduction

The enhancement of the light-matter interaction is a key point to exacerbate the optical response of a given structure leading to an increase in its performance [1, 2]. To this end, two conditions must be fulfilled: first, the increase in the lifetime of photons within the structure corresponding to the excitation of resonances with a high-quality factor (Q-factor), and second, the resonance must provide a strong confinement of the electromagnetic field at the sub-wavelength scale (small mode volume). The combination of these two conditions leads to resonance with a large Purcell factor [3]. Otherwise, plasmonic resonances [4] are probably not suitable in this context due to the involved intrinsic absorption of used metals. Thus, nowadays, most research teams focus on dielectric structures [5] fulfilling the two conditions mentioned above. This can be achieved quite easily in some specific cases, such as the excitation of a frozen mode within a photonic crystal [6], a Fano-like resonance mode [7], a Guided Mode Resonance (GMR) [8] or, more recently, a Bound state In the Continuum (BIC) [9]. In the latter case, these modes can be interpreted as non-radiative, resulting from destructive interference between two or more leaky modes, and are therefore not visible in optical spectra [10]. A typical example of such modes is the family of Symmetry Protected Modes (SPMs) [11]. The non-radiative character (dark modes) corresponds to resonance with an infinite Q-factor [9]. Symmetry breaking allows to excite such modes with a Q-factor all the more important as the degree of symmetry breaking is low [12]. The symmetry is often geometrical (with respect to a specific axis or plane combined with an illumination having the same symmetry) but can also be of electromagnetic origin (the geometrical symmetry is

preserved but with illumination having a different axis/plane of symmetry than the grating) [10]. BICs take part in many applications due to the extreme light confinement on a small scale, and their high sensitivity toward small external variations such as the refractive index of the medium. Typical applications include the enhancement of optical nonlinearities, where BICs can boost the efficiency of various nonlinear optical phenomena, such as THG in Si metasurfaces, or SHG in non-centro-symmetric materials [13, 14],

In this paper, we propose a 1D subwavelength grating with a very simple geometry that supports multiple BICs and SPMs in the near-infrared range. The structure has been fabricated and characterized under different illumination conditions showing multiple resonances with a nearly high Q-factor. Numerical simulations by FDTD (Finite Difference Time Domain) are in great agreement with the experimental data of transmission spectra. The calculations also show that these high Q-factor resonances are accompanied by a significant enhancement of the electric or/and magnetic fields, which demonstrate strong electromagnetic field confinement either in the superstrate (air), in the substrate (lithium niobate), or in the structured medium itself. This suggests diverse applications such as biological detection (index variations), in electro-, acoustic- or pyroelectric modulation, with the same component operating at different wavelengths and for different illuminations.

2. Proposed geometry

As previously mentioned, to obtain SP-BICs, the structure must possess a high degree of symmetry. The simplest is axial symmetry, which in the case of a 1D periodic lattice translates into plane (mirror) symmetry. Consequently, a rectangular cross-section pillar grating deposited onto a planar substrate precisely fulfills the requirement, with axial symmetry perpendicular to the substrate interface.

The substrate chosen for this application is lithium niobate (LN), selected for its set of non-linear properties that make it electromagnetically very important, mainly through modulation of its optical refractive index (Pockel's effect or pyroelectric effect) but also for SHG enhancement, in response to various external stimuli. The nano-structure consists of an array of pillars made of amorphous silicon (Si), a dielectric material with a high refractive index in the spectral range under consideration (NIR).

To operate in the vicinity of $\lambda = 1550$ nm, we performed numerical simulations using a customized FDTD code. Through the optimization of geometrical parameters, we aimed to achieve SP-BIC across the wavelength range of $\lambda \in [1200 - 1700]$ nm.

The geometrical characteristics of the structure after optimization, as depicted in Fig. 1(a), are set as follows: the gap between pillars is $w = 60$ nm, the height of pillars is $h = 350$ nm, and the lattice period is $p = 640$ nm. These specific parameters enable SP-BICs to be excited under different illumination conditions characterized by different values of θ, ψ, ϕ (see Fig. 1(a)), angles specifying the illumination properties (direction and polarization). Note that the (x, y, z) reference frame is aligned with the crystalline reference frame of the LN material, for consistency of notation.

As shown in Fig. 1(a), the LN substrate consists of an X-cut wafer, wherein the optical axis z is oriented parallel to the Si-pillars. This configuration enables us to capitalize on the maximal electro-optical coefficient r_{33} of the LN [15–17] when the incident plane wave is polarized along the z direction. Such alignment is imperative for achieving effective light-matter interaction.

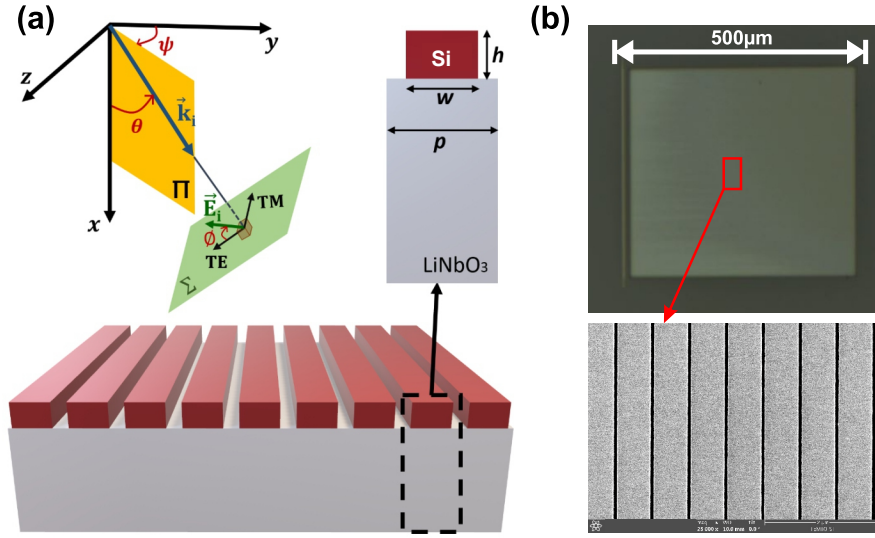


Fig. 1. (a) Illustration of the proposed grating design featuring Si-pillars atop an X-cut LN substrate. The grating parameters include the period p , pillar gap w , and pillar height h . Illumination characteristics are determined by three angles: the angles of incidence θ , azimuthal angle ψ , and the polarization angle ϕ . Π represents the plane of incidence, while Σ denotes the wavefront. (b) Scanning electron microscope (SEM) image captured from the top view of the fabricated grating, with a magnified view showcasing the central portion revealing the individual pillars.

3. Fabrication

Figure 1(b) shows two scanning electron microscopy (SEM) images of the total manufactured structure (top), and a zoom-in (down) made over the central part revealing the high quality of the manufacturing process. The latter is outlined in the flowchart presented in Fig. 2. Initially, the X-cut LN wafer is cleaned using a piranha solution [18]. Subsequently, the Si layer is deposited at room temperature via the RF magnetron sputtering technique [19]. Following this, a resist mask pattern of the Si nano-grating is formed atop the Si layer using e-beam lithography [20], employing the CSAR-13 e-beam resist from Allresist. Next, the structure undergoes deep reactive ion etching (DRIE) [21] to generate the grating patterns, followed by the removal of the e-beam mask resist using NMP solution (N-methyl-2-pyrrolidone) at 70 °C for one hour.

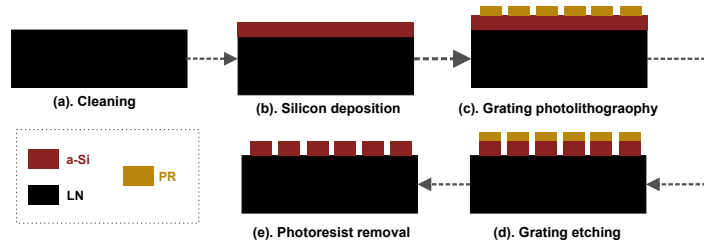


Fig. 2. Diagram and photograph of the optical bench used for transmission measurements. All elements are highlighted and indicated by yellow arrows.

The overall dimensions play a crucial role in exciting the SP-BIC [22]. Consequently, we fabricated a large-scale grating measuring $0.45 \times 0.45 \text{ mm}^2$.

4. Optical characterizations and numerical simulations

In order to measure the transmission properties of the structure, an optical bench was set up as shown in Fig. 3, where all the essential optical elements are highlighted. Two piezoelectric motor controllers were used to facilitate simultaneous manipulation of the sample for translation (C-867KO58) and rotation (KIM001). The latter is needed to vary the angle of incidence (θ), thereby facilitating the extrinsic symmetry breaking necessary for the excitation of the quasi-BICs, as we will see later. The structure is exposed to a collimated beam emitted from a fibered continuum laser source (LEUKOS-SM20-OEM). These elements are integrated into an inverted optical microscope (Olympus IX51), which has been adapted to direct a portion of the transmitted signal to an Optical Spectrum Analyzer (OSA: MS9710B Anritsu) via an optical fiber. The remaining portion of the transmitted signal is used to control the position of the incident beam relative to the grating using a CDD IR camera (Goldeye CL-033 TEC₁). The normalized transmission spectrum is obtained by dividing the signal transmitted through the structure by the signal transmitted only through the substrate; two measurements are therefore required per transmission spectrum.

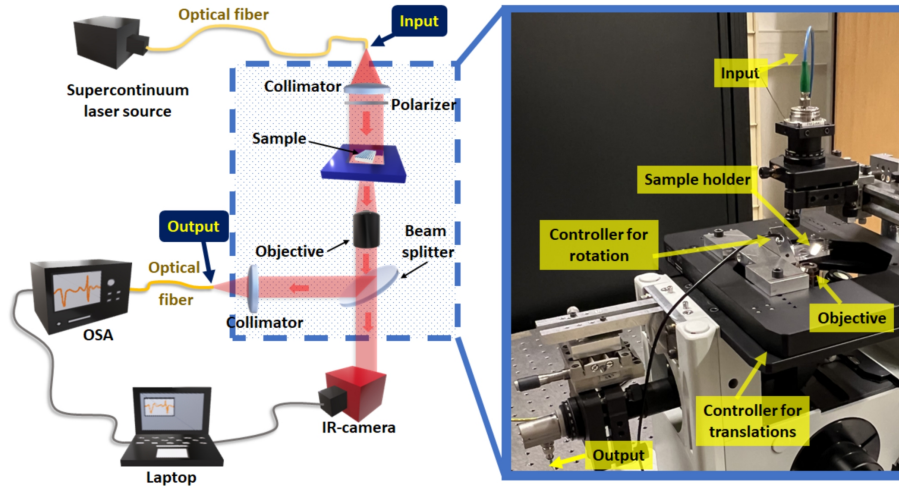


Fig. 3. Diagram and photograph of the optical bench used for transmission measurements. All elements are highlighted and indicated by yellow arrows.

As previously stated, simulations were conducted utilizing a custom FDTD code [23], enabling computation of the transmission spectrum under identical conditions as in experiment. The spatial discretization employed in the FDTD code comprises a cubic mesh with dimensions of $5 \times 5 \times 5 \text{ nm}^3$ per cell.

It is important to note that despite the structure's invariance along one direction (in this case, the O_z direction), a 2D simulation becomes inadequate due to the anisotropy of the LN material and/or in the case of azimuthal incidence ($\psi \neq 0^\circ$). Consequently, a 3D-FDTD code with periodic boundary conditions is employed, considering only one period for simulations while accounting for LN anisotropy and oblique incidence.

To address this, we have developed a custom code by integrating anisotropy into the Split-Field Method [24], enabling consideration of oblique incidence in the case of an infinitely periodic anisotropic structures.

5. Results

Four distinct configurations were examined based on the direction and polarization of the incident plane wave. To distinguish them, we define three angles as depicted in Fig. 1(a) : the azimuthal angle ψ , which specifies the angular orientation of the plane of incidence, ϕ related to the polarization angle ($\phi = 0^\circ$ for TE and $\phi = 90^\circ$ for TM) in addition to the angle of incidence θ . Hence, the four configurations studied, both numerically and experimentally, correspond to the following parameters:

Configuration (a): $(\psi, \phi) = (0^\circ, 0^\circ)$

Configuration (b): $(\psi, \phi) = (0^\circ, 90^\circ)$

Configuration (c): $(\psi, \phi) = (90^\circ, 0^\circ)$

Configuration (d): $(\psi, \phi) = (90^\circ, 90^\circ)$

However, for all configurations, the illumination is conducted from above the grating (air) with the angle of incidence θ ranging from 0 to 30° . Notably, at normal incidence, configurations (a) and (b) are respectively equivalent to configurations (d) and (c). In the former case, the electric field aligns parallel to the Si-pillars (z - axis), while in the latter, it becomes perpendicular. The optical refractive indices of LN are $n_x = n_y = n_o = 2.211$ and $n_z = n_e = 2.139$ [25]. Yet, only configuration (d) represents an anisotropic case, while both configurations (c) and (d) require 3D numerical simulations. The spectral positions of the Rayleigh anomalies are also calculated in order to better understand some features of the transmission spectra. These anomalies may interfere with other resonant modes, thereby altering their properties. In the context of 1D periodic gratings, the spectral position (λ_A) of these anomalies, which are independent of polarization, are solutions of the equation defined below [26]:

$$m^2 \lambda_A^2 + 2pn_i m \lambda_A \sin \theta \cos \psi + (n_i^2 \sin^2 \theta - \xi)p^2 = 0 \quad (1)$$

Here, m denotes the order of diffraction in the periodicity direction (y -axis), n_i is the optical refractive index of the medium of incidence (air), n_t is the optical refractive index of the medium of transmission (LN), ξ is equal to n_i^2 or n_t^2 for Rayleigh anomalies occurring in the incident or transmission medium respectively, and p is the period of the grating. In the chosen range of study, only the Rayleigh anomalies occurring in the transmission medium are visible. The solutions to Eq. 1 can therefore be expressed as follows:

When $\psi = 0^\circ$, there exist two solutions:

$$\lambda_A = \begin{cases} -\frac{p}{m} \times (n_i \sin \theta + n_t) & \text{for } m < 0 \\ -\frac{p}{m} \times (n_i \sin \theta - n_t) & \text{for } m > 0 \end{cases}$$

And when $\psi = 90^\circ$, there exists only one solution:

$$\lambda_A = \frac{p}{m} \times \sqrt{n_t^2 - n_i^2 \sin^2 \theta}$$

All the materials used behave like pure dielectrics in the near-infrared spectrum, with no absorption, enabling the quantification of the optical response of the structure, whether in transmission or reflection. Consequently, only the transmission coefficient (T) will be presented. In addition, we introduce the following parameters for the quantification of the obtained results. Firstly, the quality-factor, denoted as Q , is determined by the ratio of the resonance wavelength λ_0 to the full width at half-maximum (FWHM) $\Delta\lambda$ of a resonant peak. For resonances exhibiting Fano asymmetric line shapes, we consider the FWHM as the absolute difference between the spectral positions of the pic and the dip of the resonance. Secondly, we define the extinction ratio (ER) of the normalized transmission spectra, expressed by $ER = \frac{T_{max} - T_{min}}{T_{max}}$ where T_{max} and T_{min} represent the maximum and minimum normalized transmission intensities, respectively.

This parameter serves to evaluate the efficiency of light modulation as will be seen later. Lastly, we introduce the normalized electric and magnetic field intensities (I_e and I_m), calculated as the ratio of the intensity in the presence of both the grating and the substrate to the intensity in the presence of only the substrate. These quantities provide insight into the interaction dynamics between incident light and the grating-substrate system.

5.1. Configuration (a): $(\psi, \phi) = (0^\circ, 0^\circ)$

In this configuration, the plane of incidence (xy plane) is perpendicular to the direction of the Si-pillars (z -axis). Moreover, the E-field is oriented along the z -axis ($\phi = 0^\circ$), parallel to the Si-pillars. This corresponds to a conventional TE polarization case with no depolarization, as the plane of incidence is perpendicular to the direction of invariance (the z -axis). Consequently, the numerical simulations are entirely two-dimensional, reducing the electromagnetic field to only the (H_x, H_y, E_z) components.

Figure 4 illustrates both numerical (a) and experimental (b) results of the transmission angular diagrams. Note that the experimental ones are unprocessed raw data. Additionally, the Rayleigh anomalies of the diffracted first orders ($m = \pm 1$) are depicted by dashed blue lines in Fig. 4(a). There is excellent agreement between experience and theory (Fig. 4(a) and 4(b)) in terms of excited modes and resonance spectral positions.

Small differences can have several origins, such as the finite size of the structure and/or the illumination beam, and also the unavoidable manufacturing defects. Under normal incidence ($\theta = 0^\circ$), only the Guided Mode Resonance (GMR) is observable at the wavelength of $\lambda = 1368$ nm. However, a slight variation of the angle of incidence θ leads to a break, even slight, in the symmetry of the structure relative to the x -axis. Consequently, we observe the emergence of a Fano-shaped quasi-BIC above the $m = -1$ Rayleigh anomaly. This reveals the presence of a Symmetry Protected - Bound state in the Continuum (SP-BIC) at the point of high symmetry ($\theta = 0^\circ$).

As the angle θ increases, the GMR experiences a blue shift, whereas the quasi-BIC undergoes a red shift. For example, Fig. 4(c) illustrates the normalized transmission spectra obtained from both numerical simulation (blue dashed line) and experimental measurement (red solid line) at the angle of incidence $\theta = 9^\circ$. Within the same figure, one can observe the presence of the two resonances: the GMR one located around $\lambda = 1330$ nm and the quasi-BIC one at $\lambda = 1477$ nm. Beyond $\theta \approx 13^\circ$, the SP-BIC couples destructively with the Rayleigh anomaly of order $m = -1$. This leads to an increase in its quality factor before it disappears completely, giving rise to an accidental BIC [27].

To go further in the quasi-BIC properties, we examine a small angle of incidence, for instance, $\theta = 0.5^\circ$ for which the quasi-BIC resonates at a wavelength of $\lambda_{num} = 1438$ nm, exhibiting a substantial Q-factor of $Q_{num} = 10^6$. We numerically demonstrate that this resonance is accompanied by a significant enhancement of both electric and magnetic field intensities, with values of $I_e = 2.10^3$ and $I_m = 8.10^4$, respectively, as illustrated in Fig. 4(d). Based on these results, the quasi-BIC could be ideally suited for a wide range of integrated photonics applications, particularly in areas such as optoelectronics [11, 28] and nonlinear optics [29, 30].

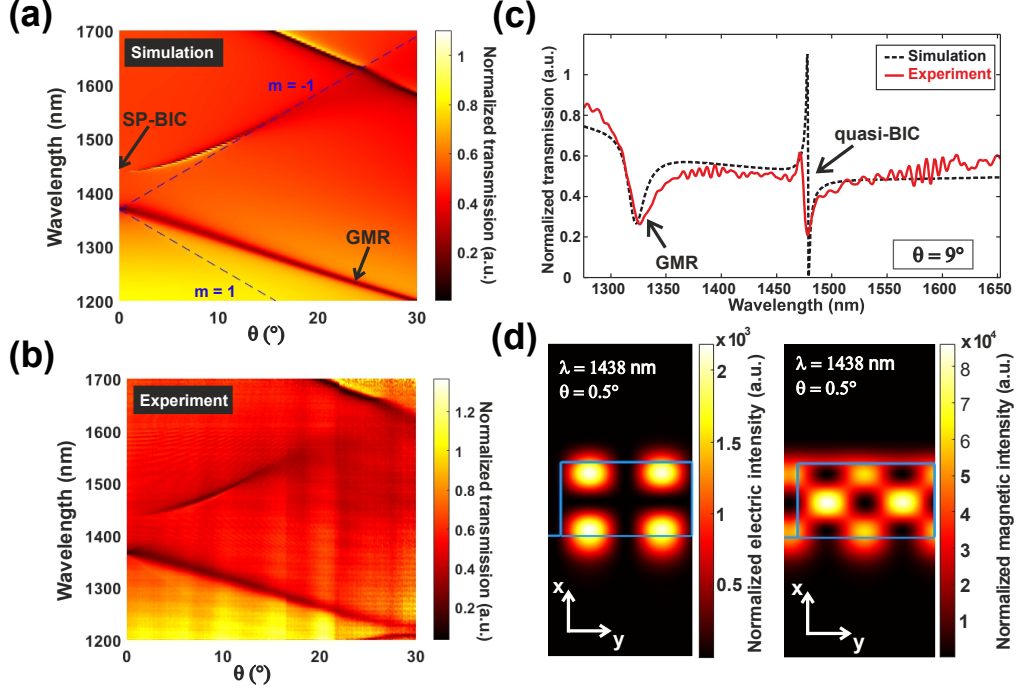


Fig. 4. (a) Transmission angular diagram obtained by FDTD numerical simulations. The dashed blue lines represent the positions of the Rayleigh anomalies for both the $m = 1$ and $m = -1$ diffraction orders. (b) Transmission angular diagram obtained from experimental measurements. (c) The transmission spectra acquired from simulation (black dashed line) and experiment (red solid line) at the angle of incidence $\theta = 9^\circ$. (d) Distributions of the normalized electric and magnetic intensities obtained from FDTD simulations at the spectral position of the quasi-BIC $\lambda = 1438$ nm for an incidence angle of $\theta = 0.5^\circ$.

The fact that the electric field of the electromagnetic wave is polarised along the LN's crystalline axis (z -axis) makes the configuration highly compatible with electro-optical or pyroelectric applications. Indeed, the largest electro-optic (EO) coefficient of the LN is $r_{33} = 31$ pm/V [31], which is mainly involved in the Pockel's effect in this case. The obtained variation in the refractive index is given by Eq. 2 [11] below.

$$\Delta n(x, y) = -\frac{1}{2} n_e^3 r_{33} f(x, y)^2 E_s \quad (2)$$

$$E_s = -\frac{1}{\epsilon_0 \epsilon_r} p_t \Delta T \quad (3)$$

Here, E_s denotes the external applied electric field magnitude, ϵ_0 and ϵ_r are, respectively, the vacuum and the LN relative dielectric constants equal to $\epsilon_0 = 8.854 \times 10^{-12}$ F/m, and $\epsilon_r = 28.7$. The function $f(x, y)$ represents the local optical field factor computed at each FDTD cell. It quantifies the electric field amplitude in the presence of the grating relative to the field amplitude in the absence of the grating. However, this refractive index modification can also be induced by a change in temperature (pyroelectric effect) which, through induced polarization, results in the generation of an electric field within the LN crystal. A relationship linking the two effects is given by Eq. 3 where p_t is the pyroelectric coefficient of the LN ($p_t = -6 \times 10^{-5}$ Cm⁻²K⁻¹), and ΔT corresponds to the temperature variation in kelvin. Let consider an external electric field

applied to the grating by integrating two electrodes deposited on the LN substrate at both ends of the grating along the z -axis. We consider a distance of $500 \mu\text{m}$ between the electrodes to cover the area of the grating since, as mentioned above, the total dimension of the grating along the z - and y -axes is $450 \times 450 \mu\text{m}^2$. Figure 5(a) depicts the local variation of the refractive index of LN induced by an external electric field of $E_s = 1.41 \text{ kV/m}$ corresponding to voltage of 0.7 V applied on the electrodes, or by temperature variation of $\Delta T = 6 \text{ mK}$.

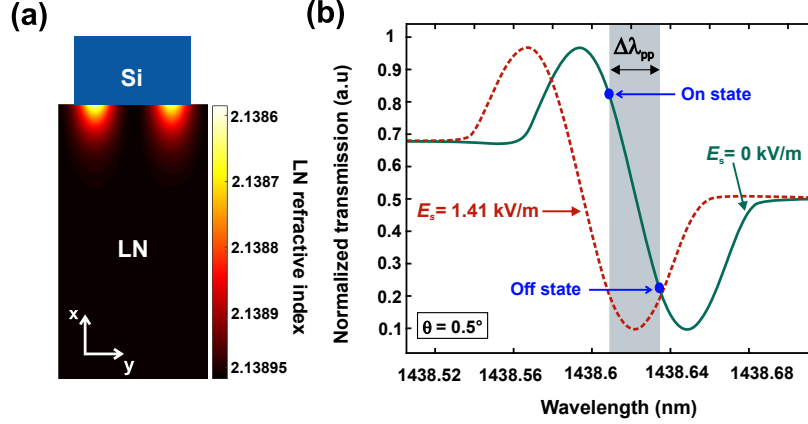


Fig. 5. (a) Spatial distribution of the LN refractive index induced by the application of an external electric field $E_s = 1.41 \text{ kV/m}$. (b) The normalized transmission response of the structure under an external electric field E_s (cases of $E_s = 1.41 \text{ kV/m}$ (red dashed line) and $E_s = 0 \text{ kV/m}$ (green solid line)).

The modification of the refractive index is then calculated through Eq. 2 for each FDTD-cell of the mesh and incorporated into the FDTD simulations to estimate the effect on the transmission response. Figure 5(b) presents the two spectra corresponding to the passive structure when $E_s = 0 \text{ V/m}$ (green solid line) and to an applied electric field of $E_s = 1.14 \text{ kV/m}$ (dashed red line). As expected, due to the large local enhancement of the electric field in the LN just above the Si-pillars, the refractive index of the latter is enough decreased allowing a large blue-shift ($\Delta\lambda_{res} = 5.26 \times 10^{-2} \text{ nm}$) of the SP-BIC resonance.

When the aim is to linearly modulate the intensity of the transmitted signal, the latter must change uniformly from an off-state to an on-state. These states, depicted by blue circles in Fig. 5(b), denote the lowest and the highest values of the normalized transmission at the quasi-BIC resonance's linear segment. This is achieved through a wavelength shift of $\Delta\lambda_{pp} = 2.24 \times 10^{-3} \text{ nm}$ corresponding to an extinction ratio of $ER = 77\%$ and a peak-to-peak drive voltage $V_{pp} = 0.7 \text{ V}$ as shown on Fig. 5(b).

Furthermore, we can assess the thermal sensitivity of the structure by exploiting the LN intrinsic pyroelectric property given by the Eq. 3. as $S_T = \Delta\lambda/\Delta T = 0.37 \times 10^9 \text{ nm/K}$. This large thermal sensitivity can be exploited for highly accurate temperature detection in the milli-Kelvin range, better than the state of the art [32–35], but can also play a negative role in other applications, then requiring correction of thermal drifts.

5.2. Configuration (b): $(\psi, \phi) = (0^\circ, 90^\circ)$

In this configuration, the plane of incidence remains the same as in configuration (a), namely perpendicular to the Si-pillars. However, the polarization state changes to a transverse magnetic (TM) with $\phi = 90^\circ$. Consequently, the electromagnetic field components are now characterized by (E_x, E_y, H_z) , where the electric field aligns with both ordinary axes (x and y), resulting in an

isotropic study case. Numerical simulations and experimental measurements of the transmission angular diagram are presented in Fig. 6(a) and Fig. 6(b) respectively. As before, the Rayleigh anomalies are also indicated by the blue dashed lines.

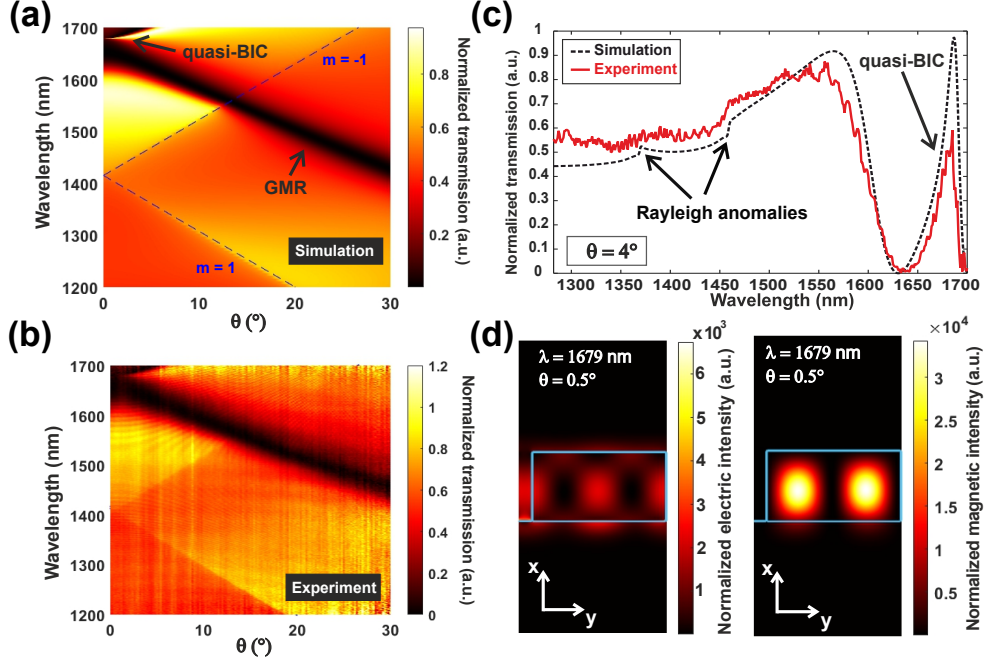


Fig. 6. (a) Transmission angular diagram derived from FDTD numerical simulations. The dashed blue lines represent the spectral positions of the Rayleigh anomalies for both the $m = 1$ and $m = -1$ diffraction orders. (b) Transmission angular diagram obtained from experimental measurements. (c) The transmission spectra acquired from simulation (black dashed line) and experiment (red solid line) at the angle of incidence $\theta = 4^\circ$. (d) Distributions of the normalized electric and magnetic intensities obtained from FDTD simulations at the spectral position of the quasi-BIC $\lambda = 1679$ nm for an incidence angle of $\theta = 0.5^\circ$.

In both diagrams, we observe the emergence of a quasi-BIC above the Rayleigh anomalies when the angle of incidence increases leading to its apparition at approximately $\lambda = 1678$ nm. The numerical and experimental normalized transmission spectra at an angle of $\theta = 4^\circ$ are illustrated in Fig. 6(c), where the quasi-BIC is located at a wavelength of $\lambda = 1686$ nm. In contrast to configuration (a), the quality factor of the SP-BIC decreases considerably with small symmetry breaks giving rise to a broadened resonance. In order to exploit it in detection, modulation, or non-linear signal generation applications, it would be necessary to operate at small incidence angles. Therefore, to quantify the confinement of the electromagnetic field, we consider an angle of incidence $\theta = 0.5^\circ$ for which the mode appears at $\lambda = 1679$ nm with a Q-factor of $Q = 892$. As depicted in Fig. 6(d), the electric intensity associated with the mode is predominantly enhanced at the surface of the LN substrate within the air cavities, reaching a maximum of $I_e = 6 \times 10^3$, along with an enhancement in magnetic intensity, mainly confined inside the Si-pillars, peaking at $I_m = 3 \times 10^4$. In particular, we observe a strong increase in magnetic intensity, probably due to the excitation of a magnetic dipolar resonance of the Si-pillars, which considerably increases the MLDOS (local density of magnetic states), opening the way to magneto-optical applications with non-absorbing structures [36, 37] other than metallic nano-antennas [38]. As mentioned

above, the electric field at resonance is significantly enhanced at the substrate interface between two Si-pillars in the gap region. This could be exploited to build a bio-sensor or refractive index detector. In this case, the superstrate is no more air but a liquid (water or blood) with refractive index n_l . FDTD simulations are then done by considering two fairly close values of n_l in order to evaluate the refractive index sensitivity of the structure in the vicinity of the quasi-BIC. Figure 7(a) shows the obtained transmission spectra in the spectral region of the quasi-BIC resonance for $n_l = 1.34$ and $n_l = 1.35$ when the angle of incidence from air on the liquid interface is fixed to $\theta = 0.75^\circ$. We can clearly see that the transmission peak is slightly shifted by $\Delta\lambda = 0.7$ nm corresponding to a weak sensitivity of 70nm/RIU, not sufficiently relevant for a refractive index detection even if the Q-factor of the resonance is almost high ($Q = 490$). Nevertheless, phase detection instead of intensity detection can, in certain configurations, greatly improve sensitivity [39]. Figure 7(b) presents the corresponding phase change induced during the transmission of light through the structure for the same two values of the refractive index (in dotted blue line for $n_l = 1.34$ and in solid black line for $n_l = 1.35$). At $\lambda = 1693.95$ nm, the phase difference, plotted in green dashed line, is maximum and is worth 23.48° which gives a good phase sensitivity of 2348 $^\circ$ /RIU. This value is considerably high [40,41], making the structure an excellent candidate for a variety of applications like label-free bio-sensing, bio-imaging, and optical filters.

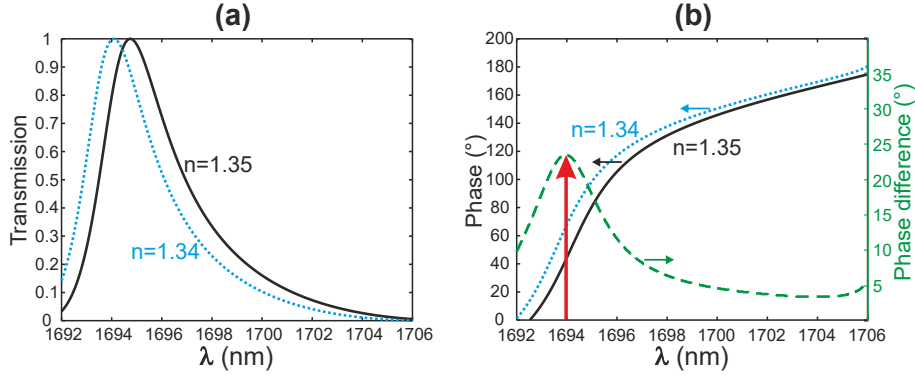


Fig. 7. (a) Transmission spectra in the region of the quasi-BIC of the structure with two different values of the refractive index n_l of the liquid superstrate ($n_l = 1.34$ in dotted blue line and $n_l = 1.35$ in solid black line). (b) Corresponding phase changes of the transmitted electric fields for the two values ($n_l = 1.34$ in dotted blue line and $n_l = 1.35$ in solid black line). The phase difference is plotted in dashed green line with a maximum value indicated by the vertical red arrow corresponding to 23.49° at $\lambda = 1693.95$ nm.

5.3. Configuration (c): $(\psi, \phi) = (90^\circ, 0^\circ)$

In this configuration, the azimuthal angle ψ is set to 90° , corresponding to a plane of incidence parallel to the xz plane and aligned with the Si-pillars. The polarization is set to $\underline{\text{TE}}$ ($\phi = 0^\circ$) so that the electric field remains perpendicular to the Si-pillars, whatever the angle of incidence. By diffraction, and due to invariance along the z direction, this electric field will give rise to a field only located in the xy plane, making the theoretical problem completely isotropic. In addition, in this configuration, as in the (d) one, changing the angle of incidence induces a very slight change in illumination conditions, so this case is rarely considered in the literature.

The numerical and experimental transmission angular diagrams are illustrated, respectively, in Fig. 8(a) and 8(b). Once again, the simulations lead to results very faithful to those obtained experimentally (see Fig. 8(c)), showing the excitation of one SP-BIC mode and one GMR. These

two modes are the same as the ones obtained in configuration (a) for the quasi-BIC, and in configuration (b) for the GMR. In fact, at normal incidence, configuration (c) is completely identical to configuration (b) while the occurrence of quasi-BIC is due to the diffraction-induced depolarization at $\theta \neq 0^\circ$ and more precisely the emergence of a non zero x-component of the electric field. As expected, the weak extrinsic symmetry break ($\theta \neq 0$) reveals this quasi-BIC at the same wavelength as in configuration (a) above the Rayleigh anomaly, as depicted in Fig. 8(c) for $\theta = 9^\circ$. The quasi-BIC resonance exhibits a good quality factor over a wide range of angle of incidence (up to $Q_{num} = 0.94 \times 10^6$ for $\theta = 0.5^\circ$), making this configuration more robust with regard to this experimental condition of illumination.

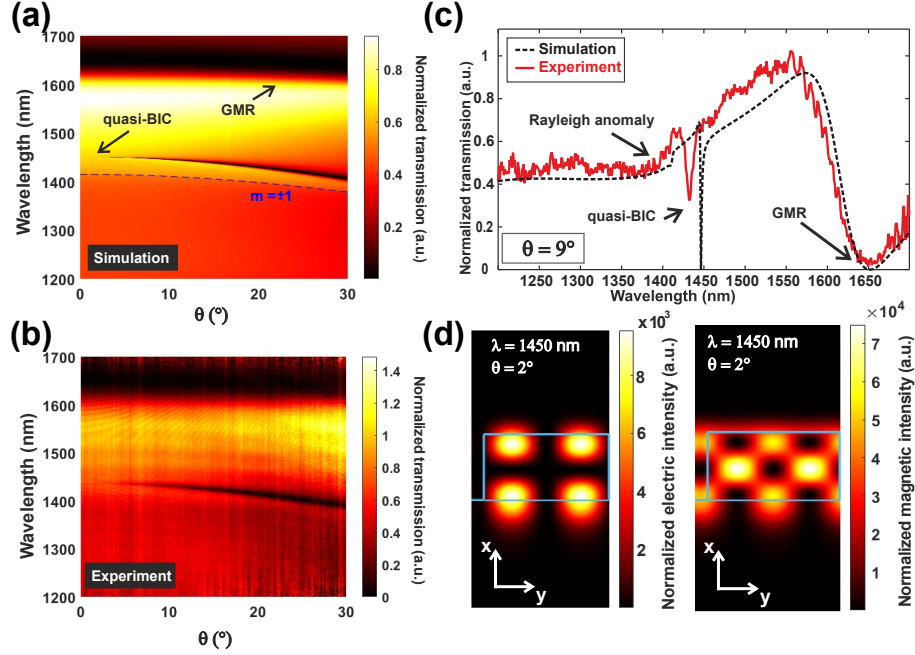


Fig. 8. (a) Transmission angular diagram derived from FDTD numerical simulations. The dashed blue line represents the spectral positions of the Rayleigh anomaly for the first diffracted order ($m = \pm 1$). (b) Transmission angular diagram obtained from experimental measurements. (c) The transmission spectra obtained from simulation (black dashed line) and experiment (red solid line) at the angle of incidence $\theta = 9^\circ$. (d) Distributions of the normalized electric and magnetic intensities obtained from FDTD simulations at the spectral position of the quasi-BIC $\lambda = 1450$ nm for an incidence angle of $\theta = 2^\circ$.

At the aforementioned quasi-BIC resonance, the electromagnetic field distributions (Fig. 8(d)) are obviously similar to those of configuration (a) (Fig. 4(d)), but with a slightly higher enhancement as shown on Fig. 8(d). The normalized electric and magnetic field intensities reach $I_e = 9 \times 10^3$ and $I_m = 8 \times 10^4$ respectively for $\theta = 2^\circ$ while similar enhancement factors need a smaller angle of incidence ($\theta = 0.5^\circ$) in the configuration (a). Nevertheless, even if the origin of the quasi-BIC is the same (Mie-type magnetic resonance) for both configurations (a) and (c), the spectral behavior with respect to the variation of the angle of incidence is different. In fact, for the (c) configuration, increasing the grating's asymmetry induces a blue-shift to the quasi-BIC while it red-shifts in configuration (a). Furthermore, the potential applications of the quasi-BIC generated in this configuration are very similar to those proposed in configuration (a) due to their similar confinement properties. However, at high incidence angles ($\theta > 4^\circ$), the

quasi-BICs of the two configurations occupy different spectral positions and can therefore be used simultaneously for the same or different applications, depending on the desired performance of each.

5.4. Configuration (d): $(\psi, \phi) = (90^\circ, 90^\circ)$

In this configuration, both angles ψ and ϕ (defined in Fig. 1(a)) are set to 90° . Therefore, the plane of incidence is the xz plane as in configuration (c) but the polarization state is TM. Consequently, the electric field is parallel to the same plane xz and has now two components along both the ordinary and extraordinary axes (x and z). The 3D-FDTD simulations must take into account this anisotropy of the configuration. The numerical and experimental transmission angular diagrams are presented in Fig. 9(a) and 9(b). As before, there is a good agreement between the two results.

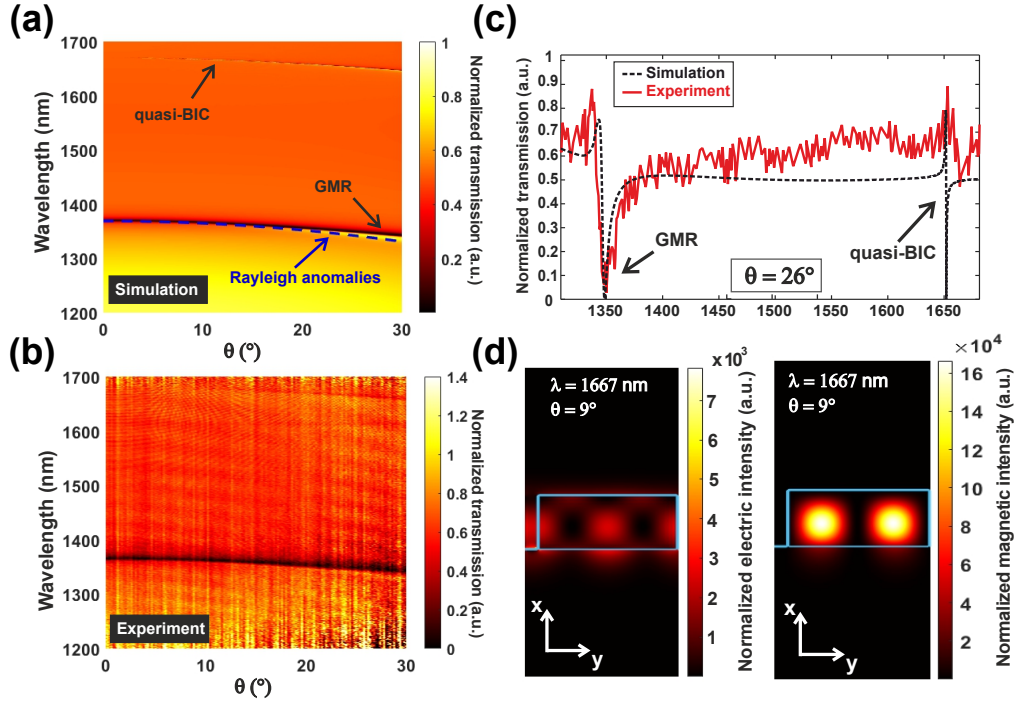


Fig. 9. (a) Transmission angular diagram derived from FDTD numerical simulations. The dashed blue line represents the spectral positions of the Rayleigh anomaly for the first diffracted order ($m = \pm 1$). (b) Transmission angular diagram obtained from experimental measurements. (c) The transmission spectra acquired from simulation (black dashed line) and experiment (red solid line) at the angle of incidence $\theta = 26^\circ$. (d) Distributions of the normalized electric and magnetic intensities obtained from FDTD simulations at the spectral position of the quasi-BIC $\lambda = 1667$ nm for an incidence angle of $\theta = 9^\circ$.

In Fig. 9(a), the dashed blue line identifies the Rayleigh anomaly corresponding to the first diffracted order ($m = \pm 1$) calculated using Eq. 1. Both diagrams emphasise the presence of two modes. However, under normal incidence, this configuration is identical to configuration (a), where a single mode exists above the Rayleigh anomalies, which is actually the GMR at $\lambda = 1370$ nm. The second mode, rather more difficult to see experimentally, only appears at $\theta \neq 0^\circ$, presenting an exceptional quality factor of $Q_{num} = 1.3 \times 10^6$ at $\theta = 0.5^\circ$, indicating a quasi-BIC state. This reveals the presence of an SP-BIC at the highest symmetry point (here Γ).

As with configuration (c), quasi-BIC maintains a significant quality factor even at higher angles of incidence. For example, at $\theta = 26^\circ$ its value remains significant, reaching $Q_{num} = 0.57 \times 10^4$, with a perfectly asymmetric Fano-shape, making this configuration of great potential for lasers and Q-switch applications. Moreover, this quasi-BIC is the same as the one excited in configuration (b) at around $\lambda = 1679$ nm and is due to depolarization, which reveals a y-component that remains fairly weak whatever the angle of incidence. Figure 9(c) illustrates the electric and magnetic intensity distributions for $\theta = 9^\circ$. As expected, these distributions are perfectly identical to those of the quasi-BIC achieved in configuration (b). However, the quasi-BIC generated in this configuration offers better confinement thanks to its high Q-factor, and has the advantage of being more robust with respect to the angle of incidence.

By observing the symmetry of the electric field distribution in Fig. 9(d), we can see that it is intimately dependent on the shape of the Si-pillar. A mechanical vibration of this pillar is therefore likely to disrupt the excitation of this quasi-BIC by shifting its excitation wavelength. This will modulate the intensity of the transmitted signal. Consequently, we investigate the structure sensitivity to such mechanical vibration, particularly relevant for acousto-optical applications [42].

A fairly simple approach is to consider a uniform tilt of the Si-pillar as shown in Fig. 10(a) where α denotes the tilt angle of the pillar with respect to the vertical direction. To estimate the influence of pillar bending, we calculated the transmission spectrum for $\alpha = 1^\circ$ (corresponding to a maximum displacement of 6.1 nm for the top of the pillar) and compared it to that of the initial structure ($\alpha = 0^\circ$). Both spectra are shown in Fig. 10(b) where the quasi-BIC undergoes a shift of $\Delta\lambda = 3.3$ nm leading to a sensitivity of $\frac{\Delta\lambda}{\Delta\alpha} = 3.3$ nm/deg. We believe that this bending is made possible by a surface acoustic wave (SAW), directed along the y-axis, and induced by an interdigital comb arranged alongside the structure, on the surface of the LN piezoelectric substrate.

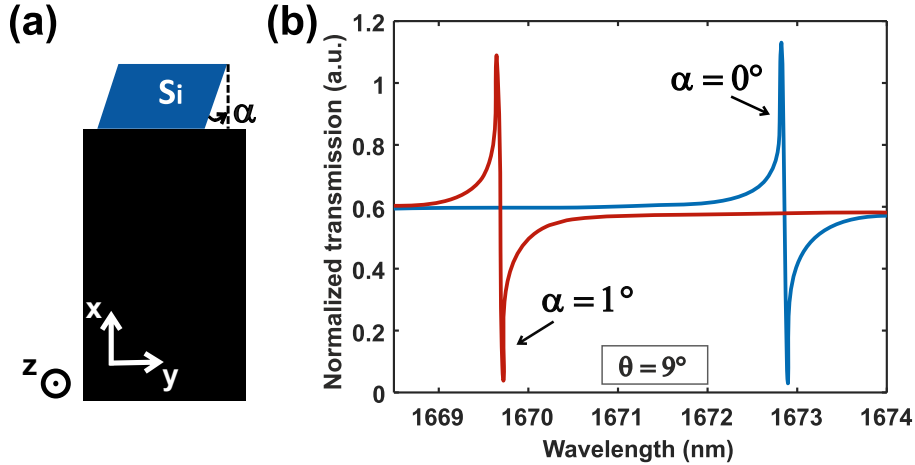


Fig. 10. (a) Diagram of a structure subjected to bending of the pillars at an angle α . (b) Comparison of the spectral position of the quasi-BIC when $\alpha = 1^\circ$ (red dashed line) versus $\alpha = 0^\circ$ (green solid line) at the angle of incidence $\theta = 9^\circ$.

6. Conclusion

We have demonstrated the ability to excite quasi-BIC modes by symmetry breaking, using four distinct configurations within the same simple-to-fabricate structure which doesn't involve lithium niobate structuring. By breaking the lattice symmetry, leakage to the SP-BIC occurs, resulting in a resonant mode (quasi-BIC) within the lattice with a particularly high Q factor.

Numerical simulations and experimental measurements show excellent agreement, confirming the reliability of the proposed structure. In each configuration, the quasi-BIC investigation was able to demonstrate the quality of the electromagnetic field confinement. We note that of the four configurations, only two SP-BICs exist, but that their coupling to the continuum can occur in two distinct ways. For example, while configurations (a) and (c) differ in various aspects such as plane of incidence, LN's refractive index and levels of symmetry breaking, they both produce quasi-BICs with similar characteristics; comparable wavelengths at low angles of incidence ($\theta \leq 0.5^\circ$) and similar field distributions, enabling its exploitation under different experimental conditions as schematically shown in Fig. 11. Similarly, configurations (b) and (d) show similarities in their quasi-BICs excited at low angles of incidence ($\theta \leq 0.5^\circ$), indicating the common origin of the SP-BIC. However, the four generated quasi-BICs show distinct responses to increasing asymmetry via the angle of incidence.

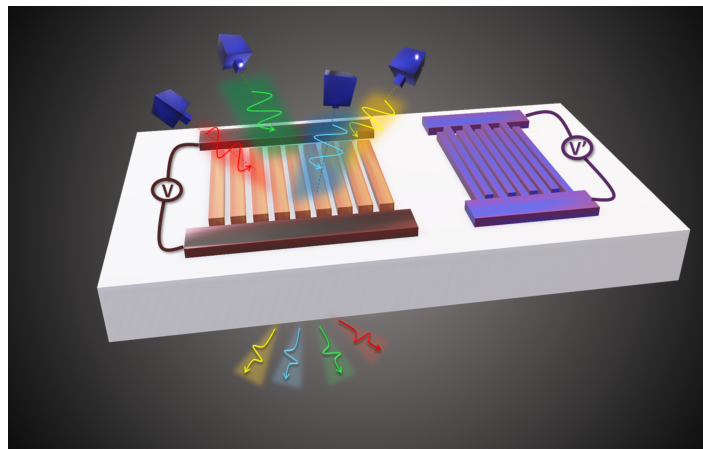


Fig. 11. Artistic illustration showing the versatility of the proposed configuration.

In addition to the compact size of the structure and the etch-free of the LN, all quasi-BICs offer significant light confinement, making the proposed structure an efficient miniaturized device for in-chip-scale applications in the NIR.

Acknowledgments

Computations have been partially performed on the supercomputer facilities of the "Mésocentre de calcul de Franche-Comté". This work has been achieved in the frame of the EIPHI Graduate school (contract "ANR-17-EURE-0002) and supported by French RENATECH network through its FEMTO-ST technological facility. The authors would like to thank Prof. Jacquot Maxime for providing the inverted microscope around which the optical bench was built.

Disclosures

The authors declare no conflicts of interest.

Data Availability

Data underlying the results presented in this paper are not publicly available at this time but may be obtained from the authors upon reasonable request.

References

1. D. Dovzhenko, S. Ryabchuk, Y. P. Rakovich, and I. Nabiev, "Light-matter interaction in the strong coupling regime: configurations, conditions, and applications," *Nanoscale* **10**, 3589–3605 (2018).
2. L. Tao, Z. Chen, Z. Li, J. Wang, X. Xu, and J.-B. Xu, "Enhancing light-matter interaction in 2d materials by optical micro/nano architectures for high-performance optoelectronic devices," *InfoMat* **3**, 36–60 (2021).
3. T. J. Kippenberg, A. L. Techebotareva, J. Kalkman, A. Polman, and K. J. Vahala, "Purcell-factor-enhanced scattering from si nanocrystals in an optical microcavity," *Phys. Rev. Lett.* **103**, 027406 (2009).
4. J. A. Schuller, E. S. Barnard, W. Cai, Y. C. Jun, J. S. White, and M. L. Brongersma, "Plasmonics for extreme light concentration and manipulation," *Nat. Mater.* **9**, 193–204 (2010).
5. S. Jahani and Z. Jacob, "All-dielectric metamaterials," *Nat. Nanotechnol.* **11**, 23–36 (2016).
6. A. Figotin and I. Vitebskiy, "Oblique frozen modes in periodic layered media," *Phys. Rev. E* **68**, 036609 (2003).
7. Y. Zhang, W. Liu, Z. Li, Z. Li, H. Cheng, S. Chen, and J. Tian, "High-quality-factor multiple fano resonances for refractive index sensing," *Opt. Lett.* **43**, 1842–1845 (2018).
8. S. Fan and J. D. Joannopoulos, "Analysis of guided resonances in photonic crystal slabs," *Phys. Rev. B* **65**, 235112 (2002).
9. D. Marinica, A. Borisov, and S. Shabanov, "Bound states in the continuum in photonics," *Phys. Rev. Lett.* **100**, 183902 (2008).
10. M.-S. Hwang, K.-Y. Jeong, J.-P. So, K.-H. Kim, and H.-G. Park, "Nanophotonic nonlinear and laser devices exploiting bound states in the continuum," *Commun. Phys.* **5**, 106 (2022).
11. A. Hoblos, M. Suarez, N. Courjal, M.-P. Bernal, and F. I. Baida, "Excitation of symmetry protected modes in a lithium niobate membrane photonic crystal for sensing applications," *OSA Continuum* **3**, 3008–3018 (2020).
12. Y. Plotnik, O. Peleg, F. Dreisow, M. Heinrich, S. Nolte, A. Szameit, and M. Segev, "Experimental observation of optical bound states in the continuum," *Phys. Rev. Lett* **107**, 183901 (2011).
13. K. Koshelev, Y. Tang, K. Li, D.-Y. Choi, G. Li, and Y. Kivshar, "Nonlinear metasurfaces governed by bound states in the continuum," *ACS Photonics* **6**, 1639–1644 (2019).
14. Z. Liu, Y. Xu, Y. Lin, J. Xiang, T. Feng, Q. Cao, J. Li, S. Lan, and J. Liu, "High-q quasibound states in the continuum for nonlinear metasurfaces," *Phys. Rev. Lett* **123**, 253901 (2019).
15. M. Roussey, M.-P. Bernal, N. Courjal, D. Van Labeke, F. Baida, and R. Salut, "Electro-optic effect exaltation on lithium niobate photonic crystals due to slow photons," *App. Phys. Lett.* **89** (2006).
16. C. Wang, M. Zhang, B. Stern, M. Lipson, and M. Lončar, "Nanophotonic lithium niobate electro-optic modulators," *Opt. Express* **26**, 1547–1555 (2018).
17. H. Weigand, V. V. Vogler-Neuling, M. R. Escalé, D. Pohl, F. U. Richter, A. Karvounis, F. Timpu, and R. Grange, "Enhanced electro-optic modulation in resonant metasurfaces of lithium niobate," *ACS Photonics* **8**, 3004–3009 (2021).
18. B. Ashe, C. Giacomini, G. Myhre, and A. Schmid, "Optimizing a cleaning process for multilayer dielectric (mld) diffraction gratings," in *Laser-Induced Damage in Optical Materials: 2007*, vol. 6720 (SPIE, 2007), pp. 225–232.
19. P. Davidse, "Theory and practice of rf sputtering," *Vacuum* **17**, 139–145 (1967).
20. M. Altissimo, "E-beam lithography for micro-/nanofabrication," *Biomicrofluidics* **4** (2010).
21. Y. Q. Fu, A. Colli, A. Fasoli, J. Luo, A. Flewitt, A. Ferrari, and W. Milne, "Deep reactive ion etching as a tool for nanostructure fabrication," *J. Vac. Sci. Technol.* **27**, 1520–1526 (2009).
22. L. Djemai, M. Hamidi, A. Mezeghrane, A. Belkhir, and F. I. Baida, "Infinite versus finite 1d-dielectric gratings supporting sp-bic modes for sensing applications," *Phys. Scr.* **99**, 025520 (2024).
23. A. Taflov, S. C. Hagness, and M. Piket-May, "Computational electromagnetics: the finite-difference time-domain method," *The Electr. Eng. Handb.* **3**, 15 (2005).
24. A. Belkhir and F. Baida, "Three-dimensional finite-difference time-domain algorithm for oblique incidence with adaptation of perfectly matched layers and nonuniform meshing: Application to the study of a radar dome," *Phys. Rev. E* **77**, 056701 (2008).
25. M. N. Polyanskiy, "Refractiveindex. info database of optical constants," *Sci. Data* **11**, 94 (2024).
26. L. Rayleigh, "On the dynamical theory of gratings," *Proc. R. Soc. Lond. Ser. A-Contain. Pap. Math. Phys. Character* **79**, 399–416 (1907).
27. C. W. Hsu, B. Zhen, J. Lee, S.-L. Chua, S. G. Johnson, J. D. Joannopoulos, and M. Soljačić, "Observation of trapped light within the radiation continuum," *Nature* **499**, 188–191 (2013).
28. J. Zhang, B. Pan, W. Liu, D. Dai, and Y. Shi, "Ultra-compact electro-optic modulator based on etchless lithium niobate photonic crystal nanobeam cavity," *Opt. Express* **30**, 20839–20846 (2022).
29. F. I. Baida, J. J. Robayo Yepes, and A. Ndao, "Giant second harmonic generation in etch-less lithium niobate thin film," *J. App. Phys.* **133** (2023).
30. X. Li, J. Ma, S. Liu, P. Huang, B. Chen, D. Wei, and J. Liu, "Efficient second harmonic generation by harnessing bound states in the continuum in semi-nonlinear etchless lithium niobate waveguides," *Light. Sci. & Appl.* **11**, 317 (2022).
31. K.-K. Wong, *Properties of lithium niobate*, 28 (IET, 2002).
32. G. Liu, S. Zong, X. Liu, J. Chen, and Z. Liu, "High-performance etchless lithium niobate layer electro-optic modulator enabled by quasi-bics," *Opt. Lett.* **49**, 113–116 (2024).
33. W. Qiu, A. Ndao, V. C. Vila, R. Salut, N. Courjal, F. I. Baida, and M.-P. Bernal, "Fano resonance-based highly

- sensitive, compact temperature sensor on thin film lithium niobate,” *Opt. Lett.* **41**, 1106–1109 (2016).
34. B. Park, I. W. Jung, J. Provine, A. Gellineau, J. Landry, R. T. Howe, and O. Solgaard, “Double-layer silicon photonic crystal fiber-tip temperature sensors,” *IEEE Photonics Technol. Lett.* **26**, 900–903 (2014).
 35. Y. Peng, J. Hou, Z. Huang, and Q. Lu, “Temperature sensor based on surface plasmon resonance within selectively coated photonic crystal fiber,” *Appl. Opt.* **51**, 6361–6367 (2012).
 36. M. Sanz-Paz, C. Ernandes, J. U. Esparza, G. W. Burr, N. F. Van Hulst, A. Maitre, L. Aigouy, T. Gacoin, N. Bonod, M. F. Garcia-Parajo *et al.*, “Enhancing magnetic light emission with all-dielectric optical nanoantennas,” *Nano letters* **18**, 3481–3487 (2018).
 37. K. Koshelev, A. Bogdanov, and Y. Kivshar, “Meta-optics and bound states in the continuum,” *Sci. Bull.* **64**, 836–842 (2019). SPECIAL TOPIC: Electromagnetic Metasurfaces: from Concept to Applications.
 38. M. Darvishzadeh-Varcheie, M. Kamandi, M. Albooyeh, and F. Capolino, “Optical magnetic field enhancement at nanoscale: a nanoantenna comparative study,” *Opt. Lett.* **44**, 4957–4960 (2019).
 39. A. V. Kabashin, S. Patskovsky, and A. N. Grigorenko, “Phase and amplitude sensitivities in surface plasmon resonance bio and chemical sensing,” *Opt. Express* **17**, 21191–21204 (2009).
 40. Y. Zhou, X. Li, S. Li, Z. Guo, P. Zeng, J. He, D. Wang, R. Zhang, M. Lu, S. Zhang *et al.*, “Symmetric guided-mode resonance sensors in aqueous media with ultrahigh figure of merit,” *Opt. Express* **27**, 34788–34802 (2019).
 41. S. Mesli, H. Yala, M. Hamidi, A. Belkhir, and F. I. Baida, “High performance for refractive index sensors via symmetry-protected guided mode resonance,” *Opt. Express* **29**, 21199–21211 (2021).
 42. Z. Yu and X. Sun, “Acousto-optic modulation of photonic bound state in the continuum,” *Light. Sci. & Appl.* **9**, 1 (2020).